ELSEVIER

Contents lists available at ScienceDirect

Journal of Colloid And Interface Science

journal homepage: www.elsevier.com/locate/jcis



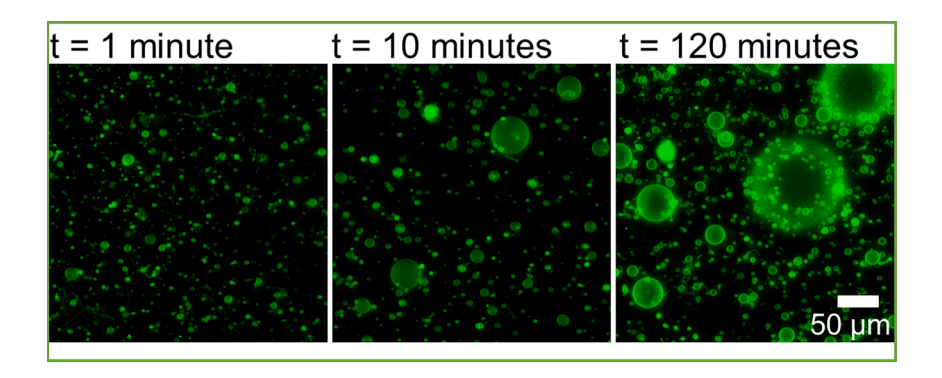
Regular Article

Dynamics of giant vesicle assembly from thin lipid films

Joseph Pazzi, Anand Bala Subramaniam

Department of Bioengineering, University of California, Merced, CA 95343, United States

G R A P H I C A L A B S T R A C T



ARTICLE INFO

Keywords:
Giant vesicles
Giant unilamellar vesicles
Thin film hydration
Electroformation
PAPYRUS
Nanocellulose
Synthetic cells
Self-assembly
Membrane dynamics
Liposomes

ABSTRACT

Motivation: Giant unilamellar vesicles (GUVs), cell-like synthetic micrometer size structures, assemble when thin lipid films are hydrated in aqueous solutions. Quantitative measurements of static yields and distribution of sizes of GUVs obtained from thin film hydration methods were recently reported. Dynamic data such as the time evolution of yields and distribution of sizes, however, is not known. Dynamic data can provide insights into the assembly pathway of GUVs and guidelines for choosing conditions to obtain populations with desired size distributions.

Approach: We develop the 'stopped-time' technique to characterize the time evolution of the distribution of sizes and molar yields of populations of free-floating GUVs. We additionally capture high resolution time-lapse images of surface-attached GUV buds on the lipid films. We systematically study the dynamics of assembly of GUVs from three widely used thin film hydration methods, PAPYRUS (Paper-Abetted amPhiphile hYdRation in aqUeous Solutions), gentle hydration, and electroformation.

Findings: We find that the molar yield versus time curves of GUVs demonstrate a characteristic sigmoidal shape, with an initial yield, a transient, and then a steady state plateau for all three methods. The population of GUVs showed a right-skewed distribution of diameters. The variance of the distributions increased with time. The systems reached steady state within 120 min. We rationalize the dynamics using the thermodynamically motivated budding and merging (BNM) model. These results further the understanding of lipid dynamics and provide for the first-time practical parameters to tailor the production of GUVs of specific sizes for applications.

E-mail address: asubramaniam@ucmerced.edu (A.B. Subramaniam).

^{*} Corresponding author.

1. Introduction

Giant unilamellar vesicles (GUVs), single walled vesicles with diameters $>1~\mu m$, are comparable in size to biological cells, mimic the chemical and physical properties of plasma membranes, and compartmentalize water soluble molecules in their lumens [1,2]. Because of these characteristics, GUVs are used widely in studies of membrane biophysics [3–8], synthetic biology [9–12], the origins of life [13–15], and in biological [16–20] and biomedical applications [21,22].

A popular class of methods to assemble GUVs is thin film hydration. In this class of methods, dry thin films of lipids on surfaces are hydrated in low salt aqueous solutions [1,2]. Variants of thin film hydration include 'gentle' or 'natural' swelling which uses glass surfaces [23,24], electroformation or electroswelling which uses conductive surfaces [25–27], gel-assisted hydration which uses glass surfaces coated with partially soluble polymers [28–30], and PAPYRUS, Paper-Abetted amPhiphile hYdRation in aqUeous Solutions, which uses nanocellulose paper [31]. Despite their wide use, an understanding of the dynamics of assembly of GUVs from these methods has remained limited. This limitation prevents rigorous mechanistic understanding and impedes the rational selection of experimental conditions to obtain GUVs with sizes desired for applications.

We recently reported an analytical framework to quantify the distribution of sizes and molar yields of populations of GUVs using confocal microscopy and large data set image analysis [31]. By standardizing experimental conditions and through statistical analysis, we showed that the molar yield of GUVs obtained using PAPYRUS was quantitatively higher than electroformation and gentle hydration [31]. We explained this result by showing that the process of assembly of GUVsized buds is thermodynamically favorable for PAPYRUS compared to electroformation and gentle hydration [31]. The surface of nanocellulose paper is composed of entangled cylindrical nanofibers while the surfaces of plain glass and indium tin oxide (ITO)-coated glass slides are flat. The free energy change for forming spherical buds from cylindrical bilayers with nanoscale radii is significantly lower than the free energy change for forming spherical buds from bilayers that are flat. The low free energy cost explains the high yield [31]. Here we develop a 'stopped-time' characterization technique to address the question of the dynamics of GUV assembly for PAPYRUS, gentle hydration, and electroformation. The stopped-time technique involves harvesting all the buds from the surfaces at specific time points. Confocal tile scan images of the resulting population of free-floating GUVs serve as an arrested time snap of the configuration of the buds on the film at the moment of harvesting. We show that the stopped-time technique allows the study of the evolution of the size distribution and the molar yield of populations of GUVs as a function of time.

We find that for all three methods, the molar yield versus time curves demonstrates a characteristic sigmoidal shape, with an initial yield, a transient, and then a steady state plateau. The yield of GUVs is similar for the three methods one minute post hydration. Then, during the transient period, the yield increases monotonically at different rates before reaching a steady state plateau at different levels and times. At steady state, the GUV yield for each method is maximized and does not change. In terms of sizes, GUVs obtained from the three methods show a right-skewed distribution of diameters ranging from 1 μm up to 150 μm. Although the total yield reaches steady state at 30 min for PAPYRUS and $60\ min$ for electroformation, the number of GUVs with diameters ${>}10$ μm continues to increase up to 120 min for both PAPYRUS and electroformation. The rate of merging decreases with time, and after 120 min, the configuration of the buds on the surface appears to be kinetically trapped. Our data shows that for PAPYRUS, obtaining maximal counts of GUVs between 10 µm and 50 µm in diameter requires 60 min of incubation and obtaining maximal counts of GUVs > 50 µm in diameter requires 120 min of incubation. For electroformation, obtaining maximal counts of both GUVs between 10 µm and 50 µm in diameter and GUVs $\geq 50~\mu m$ in diameter requires 120 min of incubation. PAPYRUS had higher absolute counts of these large GUVs compared to electroformation. Obtaining substantial numbers of GUVs $\geq 50~\mu m$ in diameter using gentle hydration was not possible. In contrast to the long incubation time needed to obtain maximal counts of large GUVs, the incubation time that maximizes the counts of GUVs $< 10~\mu m$ in diameter is remarkably short, 30 min, 1 min, and 5 min for PAPYRUS, gentle hydration, and electroformation respectively.

To obtain insights into mechanism, we capture high resolution time-lapse confocal microscopy images of the buds evolving on the surfaces. We observed three dynamical phenomena during the transient, merging of neighboring GUV-sized buds, emergence of new GUV-sized buds, and an increase in the diameter of already formed GUV-sized buds. All three dynamical processes slow with time, which explains the eventual steady state plateau in the yield and the size distribution of the GUVs. We show that the dynamics of assembly for all three methods can be explained using the thermodynamically motivated budding and merging (BNM) model of nano- and micro- scale buds.

2. Materials and methods

2.1. Materials

We purchased 75 mm \times 25 mm Fisherbrand TM premium plain glass microscope slides, 22 mm \times 22 mm glass coverslips (Gold Seal M) and 150 mm diameter Petri dishes (Falcon Bacteriological Petri Dishes with Lid) from Thermo Fisher Scientific (Waltham, MA). We purchased 25 mm \times 25 mm indium tin oxide (ITO) coated-glass slides with a surface resistivity of 8–12 Ω /sq from Sigma-Aldrich (St. Louis, MO). We purchased acid-free artist grade tracing paper (Jack Richeson & Co., Inc.) and a hole punch cutter (Amon Tech) from Amazon Inc. (Seattle, WA).

2.2. Chemicals

We purchased sucrose (BioXtra grade, purity \geq 99.5 %), glucose (BioXtra grade, purity \geq 99.5 %), and casein from bovine milk (Bio-Reagent grade) from Sigma-Aldrich (St. Louis, MO). We purchased chloroform (ACS grade, purity \geq 99.8 %, with 0.75 % ethanol as preservative) and poly(dimethyl)siloxane (Krayden Dow Sylgard 184 Silicone Elastomer Kit) from Thermo Fisher Scientific (Waltham, MA). We obtained Type I ultrapure water (resistivity \geq 18.2 M Ω ·cm) from an ELGA Pure-lab Ultra water purification system (Woodridge, IL). We purchased 1,2-dioleoyl-*sn-glycero*-3-phosphocholine (18:1 (Δ 9-cis) PC (DOPC)) and 23-(dipyrrometheneboron difluoride)-24-norcholesterol (TopFluor®-Chol) from Avanti Polar Lipids, Inc. (Alabaster, AL).

2.3. Lipid composition and concentration

The composition of the lipid mixture that we used was DOPC:Top-Fluor®-Chol at 99.5:0.5 mol %. For typical experiments, we deposit 10 μL of a 1 mg/mL solution of the lipid mixture onto 9.5 mm diameter circular pieces of paper (nominal surface concentration, NSC = 17 nmol/cm²). We deposit 10 μL of a 0.25 mg/mL solution of the lipid mixture onto 9.5 mm diameter circular pieces of paper for the sparse buds experiments (NSC = 4.25 nmol/cm²).

2.4. Stopped-time technique

We followed our previously reported protocol to clean the substrates and assemble GUVs [31]. To perform the stopped-time technique, we arrested the evolution of buds by harvesting the GUV buds at 1 min, 10 min, 30 min, 60 min, and 120 min. To harvest, we carefully disassembled the chamber by removing the top slide for gentle hydration and electroformation. We aspirated and expelled 100 μL of the hydrating solution 6 times on different regions to cover the whole substrate. After the sixth aspiration, we collected all the liquid $\sim\!150~\mu L$ containing the

GUVs and transferred the liquid into an Eppendorf tube. We constructed imaging chambers by covalently bonding custom-made square PDMS gaskets with dimensions of $6 \times 6 \times 1$ mm (width \times length \times height) to glass microscope slides. To prevent the rupture of the GUVs on the glass, we passivated the surface using a solution of 1 mg/mL case in in 1 \times PBS buffer for 1 h and then washed away the unbound casein with 3 washes of ultrapure water. We placed 58 µL of a 100 mM solution of glucose and then 2 µL of the suspension of harvested GUVs into the passivated chamber. We sealed the chamber using a glass coverslip and allowed the GUVs to sediment for 3 h before imaging. We used an upright confocal laser scanning microscope (LSM 880, Axio Imager.Z2m, Zeiss, Germany) to collect images. We excited the TopFluor® dye with a 488 nm argon laser and imaged using a 10 × Plan-Apochromat objective with a numerical aperture of 0.45. We collected 64 images covering the entire area of the chamber using an automated tile scan routine. Each tile was $850.19 \ \mu m \times 850.19 \ \mu m$ (3212 pixels \times 3212 pixels). The routine used an autofocus feature to focus $5 \mu m$ above the surface of the glass slide. To capture the equatorial plane of GUVs with diameters between 1 and 150 um, the confocal pinhole was set to 12.66 Airy Units, AU, to capture light from a slice 80 μ m in thickness. We conducted N = 3 independent repeats per time point for a total of 18 independent samples for each of the three substrates.

2.5. Image processing and analysis of tile scan data

We used a custom routine in MATLAB (Mathworks Inc., Natick, MA) to analyze the vesicles from the confocal tile scan images [31]. We applied a threshold and a watershed algorithm to segment the fluorescent objects from the background. We obtained the equivalent diameters and the mean intensities of each of the segmented objects using the native *regionprops* function. We selected objects based on the coefficient of variation

(CV) of their intensity values to distinguish GUVs from non-GUV lipid structures such as multilamellar vesicles and nanotubes. Objects that fell within 1.75 times the full width at half maximum (FWHM) of the highest peak in the histogram of CV values were selected as GUVs. We collected the diameters and the counts of all the GUVs from the tile scan. We calculate the molar yield, expressed as a percentage, using Y = $100\left(\frac{2\pi mV_h}{N_AA_{h\nu}MV_{ol}}\sum_{i=1}^n d_i^2\right)$. In this equation, m is the molecular weight of the lipid, V_h is the volume of the harvested GUV suspension, N_A is Avogadro's number, A_{hg} is the headgroup area of the lipid, M is the mass of lipid deposited on the surface, V_{al} is the volume of the aliquot in the imaging chamber, n is the number of GUVs in the imaging chamber, and d_i is the diameter of vesicle i [31]. To obtain the average rate of lipid incorporation into the GUV-sized buds, we subtract the total mols of lipids in the GUV population at the plateau from the total mols of lipids in the GUV population at the 1-minute timepoint and divide this value with the time elapsed. To obtain the mols of lipid in the population we multiply Y with the mols of lipid deposited on the surface and divide by

2.6. Imaging of buds on surfaces

For the time-lapse images of surfaces with 17 nmol/cm 2 of lipids, we used a 10 \times Plan-Apochromat objective with a numerical aperture of 0.45. We collected 15 z-slices at 2.8 μ m increments starting at the surface of the substrate. We collected Z-Stacks at 5 min, 30 min, 60 min, and 120 min. The area of the images was 425 μ m \times 425 μ m, the pixel resolution was 0.265 μ m, and the pinhole was set to 0.85 AU which resulted in a slice thickness of 5.6 μ m. To obtain a 2-dimensional projection of the buds, we summed the z-slices using ImageJ (Rasband, W.S., ImageJ, U. S. National Institutes of Health, Bethesda, Maryland, USA, https://imagej.nih.gov/ij/, 1997–2018). We used a 20 \times Plan-Apochromat objective with a numerical aperture of 1.0 to observe the merging of the buds on surfaces with 17 nmol/cm 2 of lipids. We captured 150 μ m \times

 $150\,\mu m$ images $\sim\!10\,\mu m$ from the surface at an interval of 3.5 s for 7 min. We imaged two separate locations at 3 min and then at 53 min on N=3 independent samples. The pixel resolution was $0.119~\mu m$ and the confocal slice thickness was $1.5~\mu m$. For time-lapse images of nanocellulose paper with $4.25~nmol/cm^2$ of lipids, we used a $10~\times$ Plan-Apochromat objective with a numerical aperture of 0.45. The images covered an area of $340~\mu m \times 340~\mu m$ with a pixel resolution of $0.265~\mu m$, and the pinhole was set to 1~AU resulting in a slice thickness of $5.8~\mu m$. Each Z-Stack had 11~s lices and took 1~min to acquire. We summed the slices of the Z-Stacks in ImageJ to create a 2-dimensional projection of the buds. We take each time interval as the time stamp of the first slice, that is, each sum projection image was 1~min apart. Our first point in time was at 3~min which was how long it took to find the focal position and set up the time series Z-Stack after hydrating the lipid-coated paper.

2.7. Calculation of the average rate of merging

In 2-dimensional confocal images, instances of bud merging manifest as the disappearance of the fluorescent membranes separating two adjacent non-fluorescent lumens from one frame to the next. The resulting merged bud has a single continuous fluorescent boundary that encompasses the region that was previously two separate lumens. We used the point selection tool in ImageJ to mark and count the instances of merging. We estimate the average rate of merging by dividing the total number of merging events per unit area by the total time of observation.

2.8. Analysis of incorporation of lipids into buds

For buds that do not merge with their neighbors, we measured the cross-sectional area of the buds in ImageJ. We converted the area into a diameter for a given bud i, D_i , assuming the cross section was a circle and plot these values as a function of time. We obtain the average rate of lipid incorporation in a bud i, by using, Rate $=\frac{2\pi}{N_A A_{ng}}\left(\frac{D_{iplaneou}^2 - D_{i,inital}^2}{t_{planeou} - t_{initial}}\right)$. In this equation, $D_{i,planeou}$ is the diameter of the bud at the plateau, $D_{i,initial}$ is the diameter of the bud at the plateau, $t_{i,initial}$ is the initial time. For buds that show a combination of increases in diameter and merging with their neighbors, we measured the area of the merged bud at the last frame and named it Bud 1. We then moved backwards in time toward the first frame to discern which buds merged and assign parent bud identities with index of $i=1\cdots n$ where n is the total number of buds that merged to form Bud 1. We calculate the rate of lipid incorporation using a similar process to the buds that do not merge with their neighbors.

3. Results and discussion

3.1. Stopped-time technique provides images suitable for quantification of the dynamics of GUV assembly

Fig. 1 shows high-resolution time-lapse images of buds evolving on the surface of nanocellulose paper (PAPYRUS), glass slides (gentle hydration), and ITO-coated slides (electroformation). The nanocellulose paper is composed of enmeshed cylindrical nanocellulose fibers with an average radius of 17 nm and an average length of 2 μ m while the plain glass and ITO-coated glass slides are smooth and flat [31]. All the surfaces were prepared identically by drop-casting 10 μ g of the zwitterionic lipid 1,2-dioleoyl-*sn-glycero-*3-phosphocholine (DOPC) and the fluorescent sterol TopFluor® cholesterol at a mol ratio of 99.5:0.5 %. The nominal surface concentration of lipid on the surfaces is 17 nmol/cm². We find that measuring changes in the diameter and observing the emergence of new buds from these images is difficult due to the high density of buds. Further, the surface images favor large buds while small buds are obscured. In contrast, representative stopped-time images (see

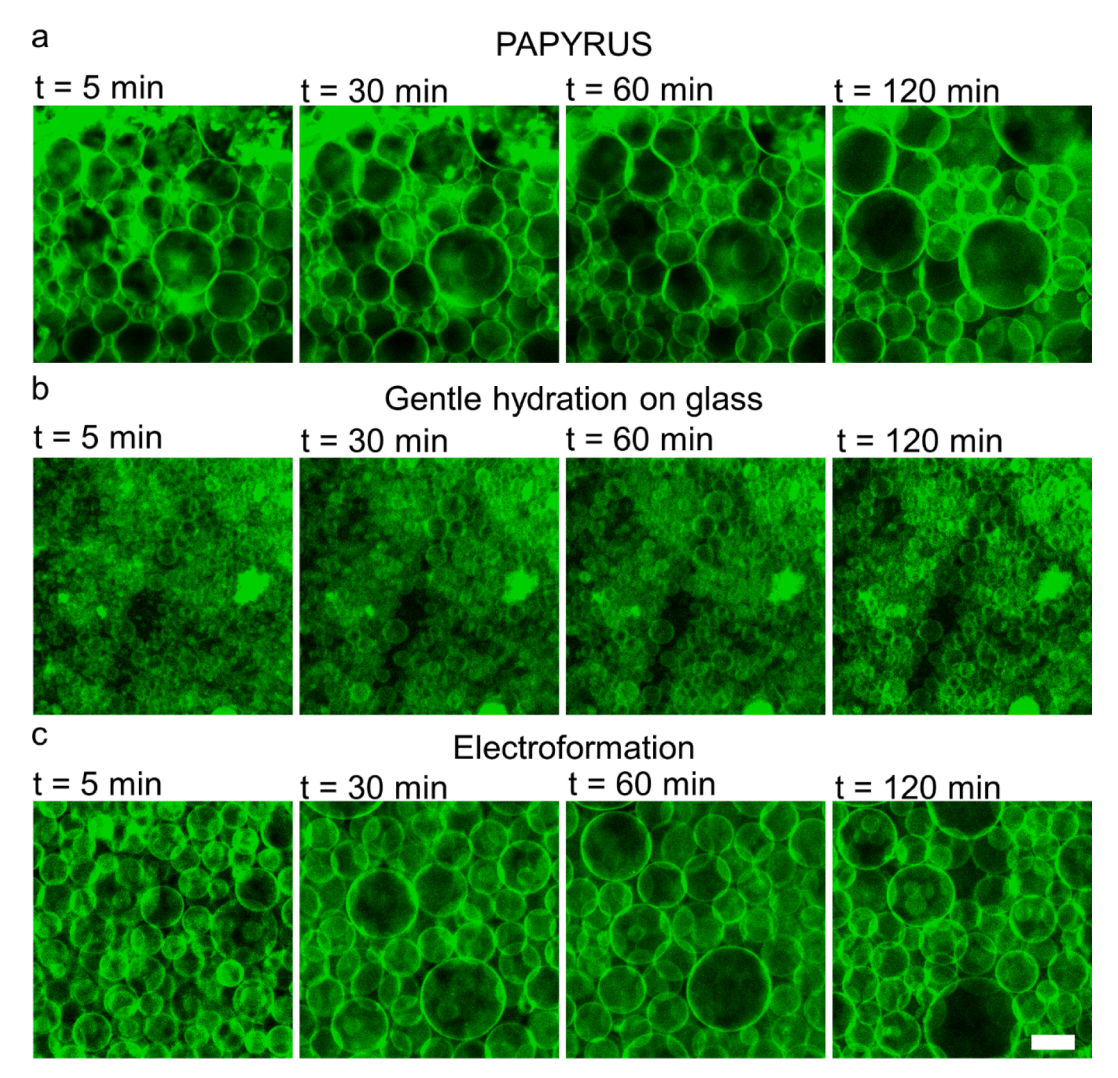


Fig. 1. Sum projections of confocal Z-Stack images showing the time evolution of buds on the surfaces. (a) PAPYRUS, (b) Gentle hydration on glass, (c) Electroformation. Because of the high density of buds that overlap in different layers, systematically counting the number of buds and measuring changes in the diameter of the buds is challenging. Scale bar 25 µm.

Materials and methods for details) at 1 min, 10 min, and 120 min show GUVs that are well separated (Fig. 2). GUVs with diameters ranging from one micrometer to hundreds of micrometers are plainly visible in the high-resolution images. Qualitatively, these images show that the number of GUVs with diameters $>\!10~\mu m$ increase with time for PAPYRUS and electroformation. Small GUVs with diameters between 1 μm and 10 μm are always present. Finding GUVs with diameters $\geq\!50~\mu m$ in typical fields of view is more common after 120 min of incubation for PAPYRUS and electroformation while finding GUVs with diameters $\geq\!50~\mu m$ is rare for gentle hydration even for samples allowed to incubate for 120 min.

3.2. Maximum GUV sizes increase with time resulting in a broadening of the distribution of sizes

We quantify the distribution of diameters and the number of GUVs from the tile scan images. Fig. 3 shows histograms of the distribution of diameters of the GUVs at 1 min, 10 min, and 120 min. We show the histograms for 5 min, 30 min, and 60 min in Figs. S1, S2, and S3 (Supporting Information). The bin width is 1 μm and each bin is an average of the N=3 independent experiments. We normalize the counts by the lipid mass deposited on the substrates.

All the samples show broad and strikingly asymmetric distributions of diameters for all time points. Asymmetric distributions of diameters

are a common feature of GUVs obtained through thin film hydration methods such as from glass [24,31,32], electroformation [33], fabric [34], filter paper [35], and gel-assisted hydration [30]. In all samples and for all times, GUVs of small diameters are more abundant than GUVs of large diameters. Thus, there is no characteristic diameter of GUVs.

We find that the distributions cannot be fit with common probability distributions, such as a Gaussian, exponential, gamma, Weibull, or lognormal distribution. These distributions are used to describe the sizes of dispersed particles that arise from classical nucleation and growth [36], coarsening [37], coalescence and fragmentation [38], and the assembly of nanoscale liposomes in bulk solution [39]. Thus, to obtain further insight into the dynamics of the evolution of the counts of GUVs, we divide our data into population classes based on diameter. Fig. 4a–c shows the counts of GUVs with diameters, d, between 1 μ m $\leq d < 10 \mu$ m, Fig. 4d–f shows the counts of GUVs with diameters between 10 μ m $\leq d < 50 \mu$ m, Fig. 4g–i shows the counts of GUVs. We chose these population classes because GUVs between 1 μ m $\leq d < 10 \mu$ m are of the sizes of blood cells, intracellular organelles, and bacteria and GUVs between 10 μ m $\leq d < 50 \mu$ m are of the size of mammalian cells.

We find that the counts of GUVs $<10~\mu m$ in diameter shows non-monotonic behavior with time for PAPYRUS and electroformation (Fig. 4a,c), whereas the counts of GUVs $<10~\mu m$ in diameter decreases monotonically with time for gentle hydration (Fig. 4b). Unlike the

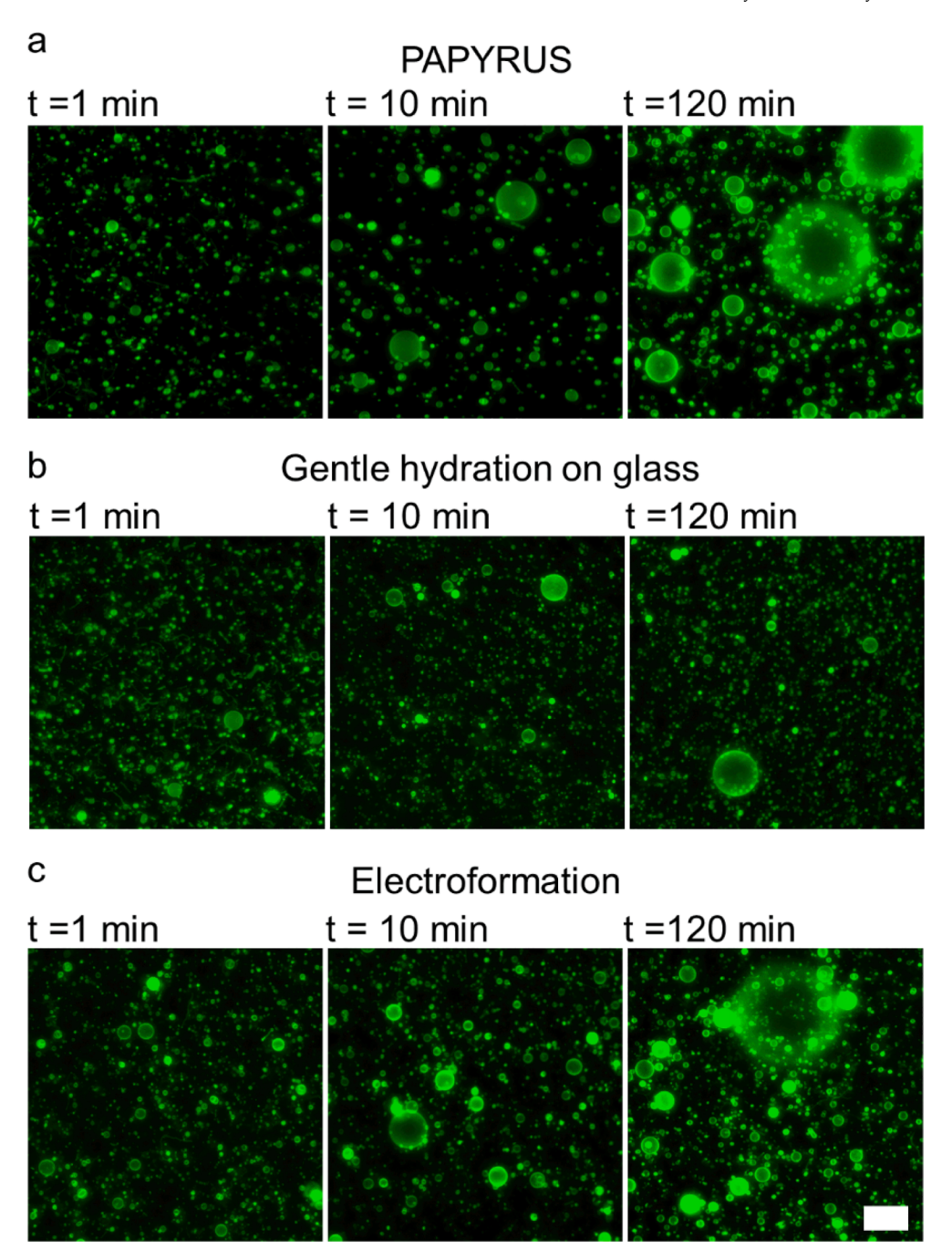


Fig. 2. Representative stopped-time images of GUVs at different time points. The confocal pinhole was left open to capture light from a slice $80 \mu m$ in thickness. (a) PAPYRUS, (b) gentle hydration, (c) electroformation. GUVs with large diameters become more abundant with time while small GUVs are always present. Scale bar $50 \mu m$.

evolution of GUVs < 10 μ m in diameter, the counts of GUVs between 10 μ m $\leq d < 50 \,\mu$ m and $d \geq 50 \,\mu$ m showed largely monotonic increases with time (Fig. 4d–i) for all three methods. The counts of GUVs between 10 μ m $\leq d < 50 \,\mu$ m and $d \geq 50 \,\mu$ m reaches a plateau within 120 min for PAPYRUS and electroformation. Of the three methods, PAPYRUS produces the highest counts of GUVs $\geq 50 \,\mu$ m in diameter and gentle hydration the lowest. The evolution of the total counts of GUVs, however, is dominated by the counts of GUVs $< 10 \,\mu$ m in diameter since they are more abundant than GUVs $> 10 \,\mu$ m in diameter (Fig. 4j–l).

Looking at the summary statistics of the distributions (Table 1), the median diameter increased by less than 1 μm for all three methods, from 2.8 \pm 0.3 μm to 3.6 \pm 0.2 μm for PAPYRUS, 2.3 \pm 0.1 μm to 2.9 \pm 0.3 μm for gentle hydration, and 2.6 \pm 0.1 μm to 2.8 \pm 0.1 μm for

electroformation. The variance of the distributions showed comparatively larger changes, from $4.0\pm0.5~\mu m^2$ to $20\pm6~\mu m^2$ for PAPYRUS, $3.1\pm0.4~\mu m^2$ to $8\pm2~\mu m^2$ for gentle hydration, and $3\pm1~\mu m^2$ to $13\pm1~\mu m^2$ electroformation. Overall, PAPYRUS showed the largest change in the median diameter and the variance and gentle hydration showed the smallest change. The evolution of the variance is consistent with the broadening of the distribution due to the largely monotonically increasing counts of GUVs $\geq10~\mu m$ in diameter with time. Despite the increasing counts of GUVs $\geq10~\mu m$ in diameter, the much larger numbers of GUVs $<10~\mu m$ in diameter results in a small net change in the median diameter of the population.

To summarize, our data shows that obtaining maximal counts of GUVs $\geq 10~\mu m$ in diameter requires 120 min of incubation for

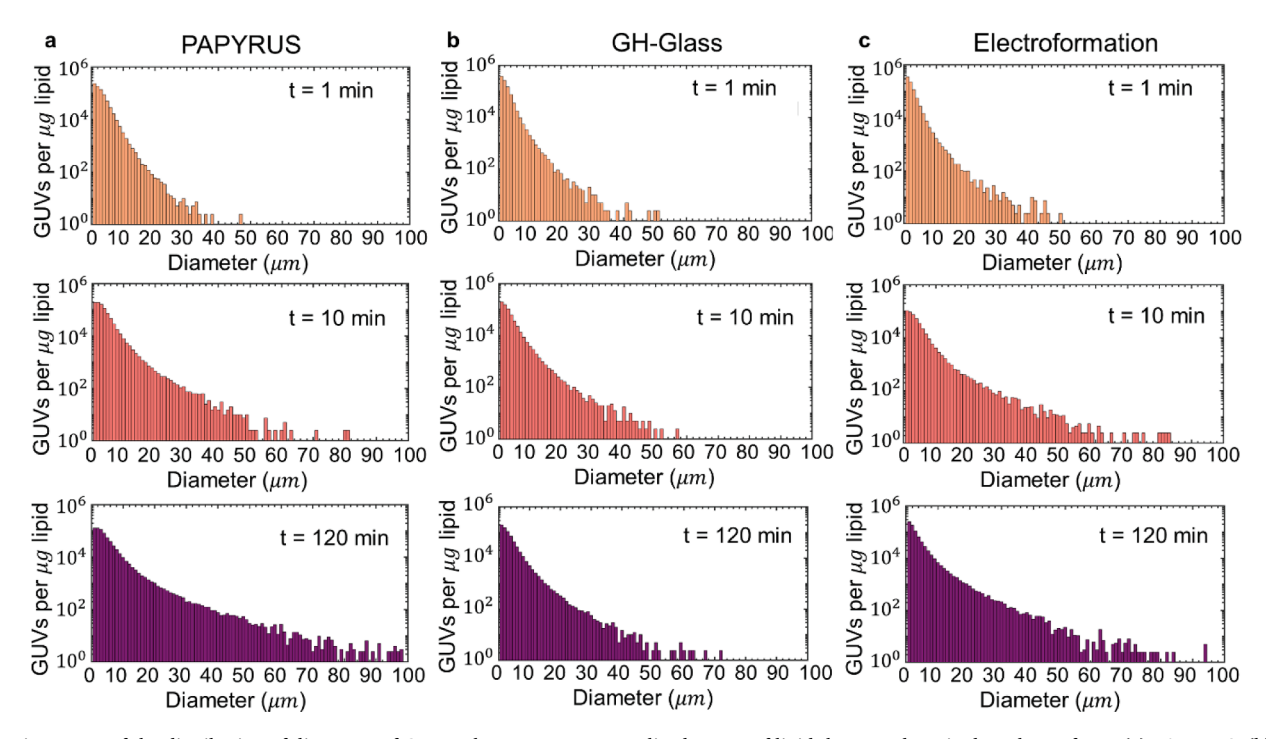


Fig. 3. Histograms of the distribution of diameters of GUVs. The counts are normalized per μ g of lipid that was deposited on the surfaces. (a) PAPYRUS, (b) gentle hydration on glass, (c) electroformation. The inset shows the stopping time. The bin widths are 1 μ m. Each bar represents an average of N=3 independent experiments. Note the log scale on the y-axis.

electroformation and PAPYRUS. In contrast, obtaining GUVs $<10~\mu m$ in diameter does not require long incubation times. The optimal incubation time to obtain GUVs $<10~\mu m$ in diameter is 30 min, 1 min, and 5 min for PAPYRUS, gentle hydration, and electroformation respectively. Obtaining substantial numbers of GUVs \geq 50 μm in diameter using gentle hydration does not appear to be possible. Extending the incubation time to 3 h does not change these results (Figs. S4, S5, Supporting Information). These results are useful for optimizing the incubation time to obtain GUVs of a desired diameter and places an upper limit on the diameter of GUVs that can be obtained from each method.

3.3. GUV molar yields plateau within 60 min while coarsening of sizes proceeds for an additional 60 min

Having characterized the evolution of the size distribution and GUV counts with time, we next consider the evolution of the molar yield of GUVs with time. The molar yield measures the moles of lipid in the membranes of the population of harvested GUVs relative to the moles of lipids that were initially deposited on the surface [31]. Drawing an analogy to chemical synthesis, the amount of lipid per unit area deposited onto the surface is the concentration of the reactant and the amount of lipid in the membranes of the harvested GUVs is the product. An increase in the molar yield indicates that more of the reactant has been converted into the product. Thus, the molar yield versus time curve for GUVs is analogous to a yield versus time curve of a chemical product. We describe the details for calculating the molar yield from confocal tile scan images in the Materials and methods.

Fig. 5a–c shows stacked area plots of the molar yield versus time. the areas represent the portion of the yield that is comprised of GUVs 1 $\mu m \leq d < 10~\mu m$, dark blue, GUVs 10 $\mu m \leq d < 50~\mu m$, light blue, and GUVs $d \geq 50~\mu m$, white. Note that although GUVs $\geq 10~\mu m$ in diameter comprise less than 10 % of the population on a per count basis at 120 min for all three methods, they make up to $\sim\!60~\%, \sim\!33~\%$, and $\sim\!54~\%$ of the total yield of GUVs from PAPYRUS, gentle hydration, and electroformation respectively.

The total molar yield versus time curves is sigmoidal for all three

methods. The molar yield of GUVs increases monotonically with time in a transient period before reaching a steady state plateau. At the plateau, the yield is maximized and does not change, that is, at the plateau, no new lipid incorporates into the GUV-sized buds from the lipid films.

The yield at 1 min is largely similar for the three methods, $13\pm1\%$, $12\pm2\%$, and $9\pm1\%$, for PAPYRUS, gentle hydration, and electroformation respectively. During the transient, the average rate of lipid incorporation was highest for PAPYRUS at 7.7×10^{-11} mol min $^{-1}$ and lowest for gentle hydration at 4.7×10^{-12} mol min $^{-1}$ Electroformation had an intermediate rate of lipid incorporation at 2.8×10^{-11} mol min $^{-1}$. These differences in rates are reflected in PAPYRUS reaching its steady state faster and plateauing at a higher value than gentle hydration and electroformation. The molar yield plateaus at $31\pm1\%$ at 30 min for PAPYRUS and at $22\pm1\%$ at 60 min for electroformation. Gentle hydration on glass plateaus at 60 min. However, unlike the other two methods, the yield at the plateau is $16\pm2\%$ which is only 4% higher than the initial yield. In contrast, the difference between the initial yield and the yield at the plateau for PAPYRUS and for electroformation is 18% and 13% respectively.

After reaching a plateau in total yield, the proportion of lipids in GUVs between 1 $\mu m \leq d < 10~\mu m$ decreases while the proportion of lipids in GUVs $10~\mu m \leq d < 50~\mu m$ and $d \geq 50~\mu m$ increases between 60 min and 120 min for both PAPYRUS and electroformation. From this observation, we deduce that the amount of lipid in GUVs $\geq 10~\mu m$ in diameter increases at the expense of GUVs $< 10~\mu m$ in diameter. Since the distribution of lipids shifts towards the population of GUVs with large diameters without any increase in the total molar yield, we classify this behavior as coarsening of the GUV buds.

We plot the molar yield of GUVs $\geq 10~\mu m$ in diameter versus the total molar yield of GUVs to illustrate graphically the differences in dynamics between the methods (Fig. 5d–f). In these plots, the x and y error bars are one standard deviation from the mean and the gray dashed line is where half of the lipid molecules are in GUVs $\geq 10~\mu m$ in diameter. The orange lines with arrowheads trace the progression of time. Movement in the positive direction parallel to the x-axis shows incorporation of lipid from the film into the population of GUV-sized buds. Incorporation of lipid

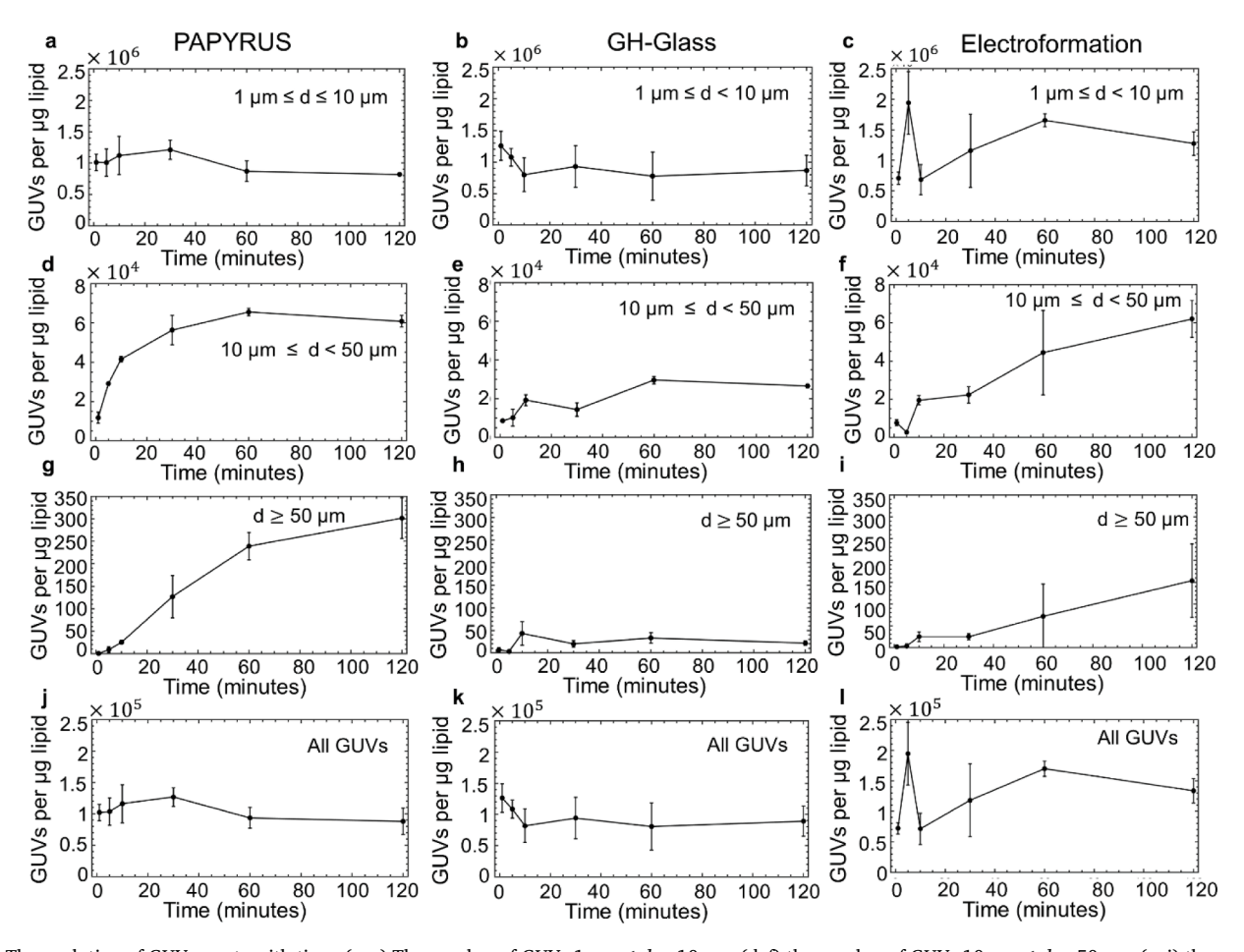


Fig. 4. The evolution of GUV counts with time. (a–c) The number of GUVs 1 μ m $\leq d < 10 ~\mu$ m, (d–f) the number of GUVs 10 μ m $\leq d < 50 ~\mu$ m, (g–i) the number of GUVs $d \geq 50 ~\mu$ m and (j–l) the total number of GUVs. Each data point is an average of N=3 independent experiments. The error bars show one standard deviation from the mean.

Table 1 Median diameter and variance of GUVs obtained from PAPYRUS, gentle hydration, and electroformation at different time points. Each value is an average of $N\,=\,3$ independent repeats. The error is one standard deviation from the mean.

Time (min)	PAPYRUS		Gentle hydration		Electroformation	
	Median (μm)	Variance (μm²)	Median (μm)	Variance (μm²)	Median (μm)	Variance (μm²)
1	2.8 ±	4.0 ± 0.5	2.3 ±	3.1 ± 0.4	2.6 ±	3 ± 1
	0.3		0.1		0.1	
5	3.3 \pm	7 ± 1	2.3 \pm	3.4 ± 0.5	2.0 \pm	2 ± 1
	0.2		0.1		0.1	
10	$3.3~\pm$	9 ± 2	$2.7~\pm$	8 ± 3	$2.6 \pm$	10 ± 1
	0.2		0.1		0.3	
30	3.4 \pm	11 ± 2	$2.5 \pm$	6 ± 1	2.5 \pm	7 ± 2
	0.3		0.1		0.1	
60	3.6 \pm	17 ± 2	$3.0 \pm$	10 ± 3	2.5 \pm	7 ± 3
	0.4		0.5		0.1	
120	$3.6 \pm$	20 ± 6	$2.9 \pm$	8 ± 2	2.8 \pm	13 ± 1
	0.2		0.3		0.1	

occurs either through the formation of new buds ${<}10~\mu m$ in diameter or through an increase in the diameter of the buds without changing the proportion of lipids in buds ${\geq}10~\mu m$ in diameter. Movement in the positive direction parallel to the y-axis shows coarsening of the buds to form buds of large diameters without incorporating lipid from the film into the population of GUV-sized buds. Diagonal movements on the plots show both the incorporation of lipid and an increase in the diameter of the buds.

These plots illustrate the fundamental differences in the dynamics of the buds for the three methods. PAPYRUS shows a period of both incorporation of lipid and increase in bud diameters for the first 30 min and a period of significant coarsening without lipid incorporation between 30 and 60 min. Only minimal coarsening occurs from 60 to 120 min. Gentle hydration shows both limited incorporation of lipid and limited increase in bud diameters, evident from the short path length of the arrows. The time trace is more complex for electroformation compared to the other two methods. Electroformation shows a period of both lipid incorporation and increases in bud diameter from 1 to 10 min and then again from 30 to 60 min. From 10 to 30 min, lipids incorporate into the population of GUV-sized buds with a minimal increase in bud diameters. Finally, from 60 to 120 min, GUV-sized buds coarsen with no incorporation of lipid.

3.4. At typical lipid concentrations only merging of GUV-sized buds is visible on the surfaces

To further understand the local dynamics of the buds that give rise to the population-level data, we imaged the evolution of the buds on the surfaces using high-resolution confocal microscopy. At the typical concentration of 17 nmol/cm 2 of lipids on the surface, micrometer-sized GUV buds are abundant and close-packed on the surfaces of nanocellulose paper and ITO-coated slides (Fig. 1). Buds are less abundant on the glass slides. Fig. 6a shows a depth-coded x-y and x-z reconstruction of the buds on a piece of lipid-coated nanocellulose paper after 60 min of incubation. The buds appear as 5–6 layers stratified by size. Due to the large differences in the sizes of the buds, buds 1 to 5 μ m in diameter

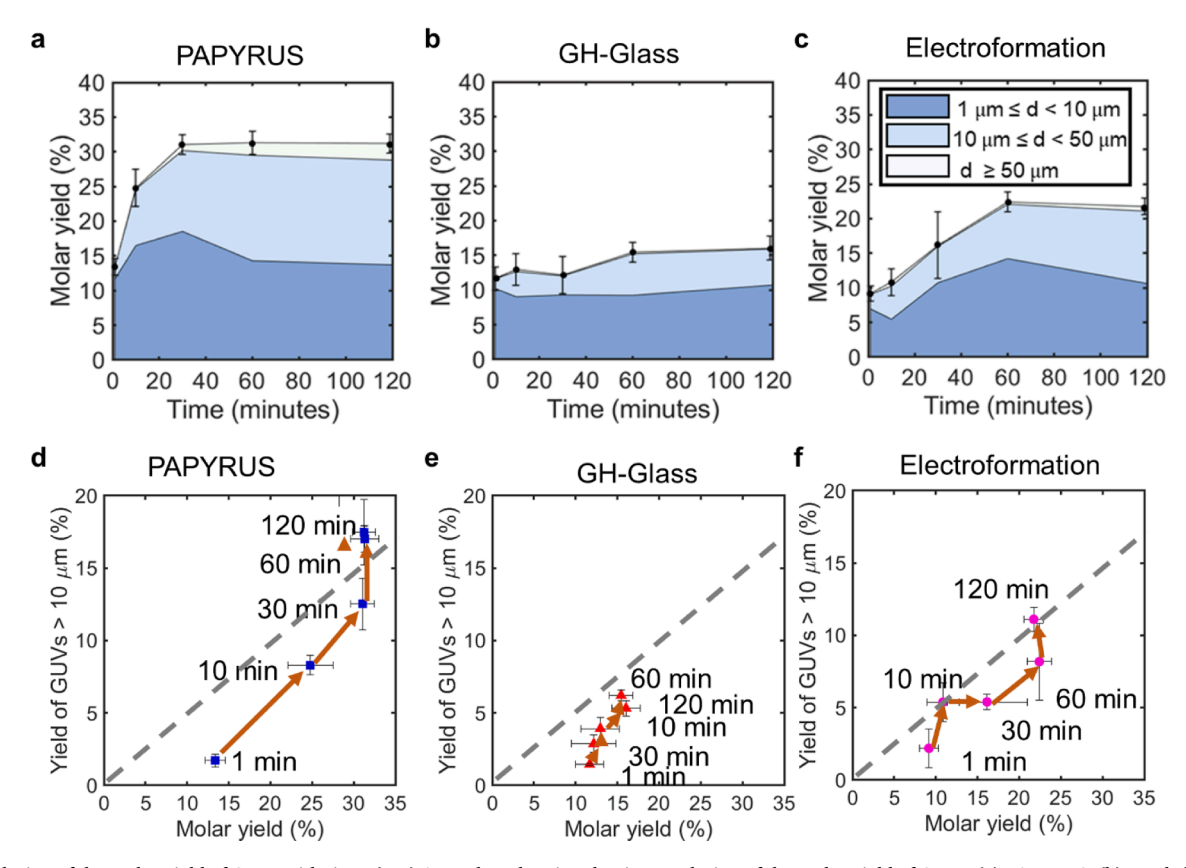


Fig. 5. Evolution of the molar yield of GUVs with time. (a–c) Area plots showing the time evolution of the molar yield of GUVs. (a) PAPYRUS, (b) gentle hydration on glass, (c) electroformation. The areas show the percentage of the molar yield that is comprised of the different size classifications listed in the legend. (d–f) Scatter plots showing the molar yield of GUVs $\geq 10 \, \mu m$ in diameter versus the total molar yield. (d) PAPYRUS, (e) gentle hydration on glass, (f) electroformation. The orange arrows show the progression of time. Each point is an average of N=3 independent experiments. The error bars show one standard deviation from the mean.

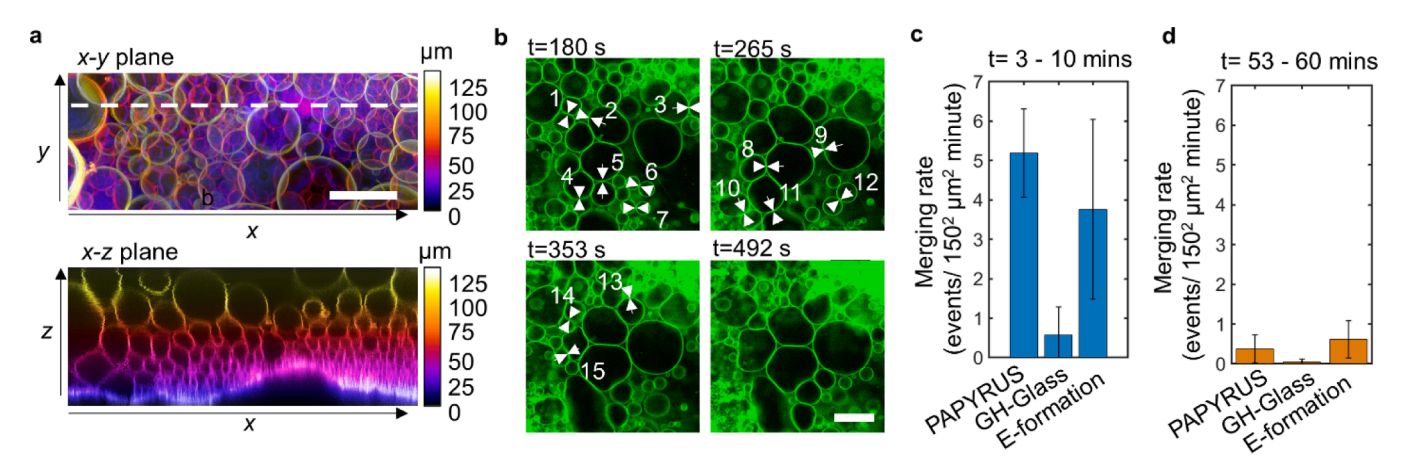


Fig. 6. *In situ* analysis of buds on the surface. (a) Three-dimensional configuration of the buds on the surface. The upper panel shows a color-coded x-y projection using the sum slices method of the buds from a confocal Z-Stack. The lower panel shows an orthogonal x-z projection of the region indicated by the dashed line in the upper panel. The white layer at the bottom are high densities of small buds on the surface of the paper. (b) Stills showing merging between buds. The white numbered arrowheads show the membranes that rearranged, which led to the merging of the adjacent buds. (c) The number of merging events between 3 and 10 min after hydration. (d) The number of merging events between 53 and 60 min after hydration. Each bar is an average of N = 3 different experiments. The error bars show one standard deviation from the mean. Scale bar 20 μm.

appear closer to the surface and buds $>\!5~\mu m$ in diameter appear further away from the surface. The thickness of the overall layer of buds is $\sim\!150\text{--}200~\mu m$. Reflective of their lower yields compared to PAPYRUS, buds appear as two layers on the surface of ITO-coated slides and buds appear as a single layer on the surface of the glass slides.

We obtained time-lapse images of the bud layer by focusing on a single z-plane 1.5 μm in thickness approximately 10 μm from the

surfaces. The primary dynamical phenomena that we observe is merging of the surface-attached GUV buds. We estimate the rate of merging by imaging for a period of 7 min between 3 and 10 min after hydration and between 53 and 60 min after hydration. Fig. 6b shows a characteristic sequence of images of buds on nanocellulose paper (PAPYRUS) during the former period. We do not show the latter period because the buds show minimal changes.

Fig. 6c,d shows a bar plot of the number of merging events that occur during the two observation periods. Between 3 and 10 min, PAPYRUS had the highest number of merging events at 5 events per 22,500 μm^2 per minute, followed by electroformation at 4 events per 22,500 μm^2 per minute. Gentle hydration had the lowest number of merging events at 0.5 events per 22,500 μm^2 per minute. Between 53 and 60 min, the rate of merging decreased to below one event per 22,500 μm^2 per minute for all three methods (Fig. 6d). These results show that merging is more prevalent for PAPYRUS and electroformation compared to gentle hydration and that the rate of merging decreases over the 1-hour period for both PAPYRUS and electroformation.

The merging of micrometer-sized GUV buds does not increase the total amount of lipid in the GUV population. Since the stopped-time data shows periods of increase in the yield, we surmise new buds must emerge and buds must increase in diameter through mechanisms other than merging with neighboring GUV-sized buds. However, we could not discern these dynamical phenomena on these surfaces that have a high density of buds.

3.5. Samples with sparse buds show emergence of new GUV buds and lipids incorporating into existing GUV buds

To make progress, we prepared surfaces with sparse coverage of GUV buds by depositing four times less lipid on the surface, 4.25 nmol/cm². We focused on the PAPYRUS method since it produced the highest yield of GUVs. We obtained detailed two-dimensional projections from the three-dimensional Z-Stacks that capture the dynamics of the buds. Fig. 7a shows the surface 3 min after hydration and Fig. 7b shows the surface 60 min after hydration. Most of the buds appear in clusters. There were few isolated buds. Within the clusters, we could identify buds $>5~\mu m$ in diameter while buds $<5~\mu m$ in diameter were poorly resolved. We could discern buds $>3.5~\mu m$ in diameter when they were isolated. At 3 min, there were many regions of high fluorescence intensities within the clusters. We show a magnified image of one such region in Fig. 7c. At 60 min, the regions of high fluorescence intensities appear to be GUV buds $>5 \, \mu m$ in diameter (Fig. 7d). We thus interpret that the regions of high fluorescence intensities are clusters of small buds $< 5 \,\mu m$ in diameter that then subsequently evolved to become buds > 5 µm in diameter.

For analysis, we selected six individual buds that do not appear to merge with their neighbors (numbered 1–6, colored boxes in Fig. 7a,b).

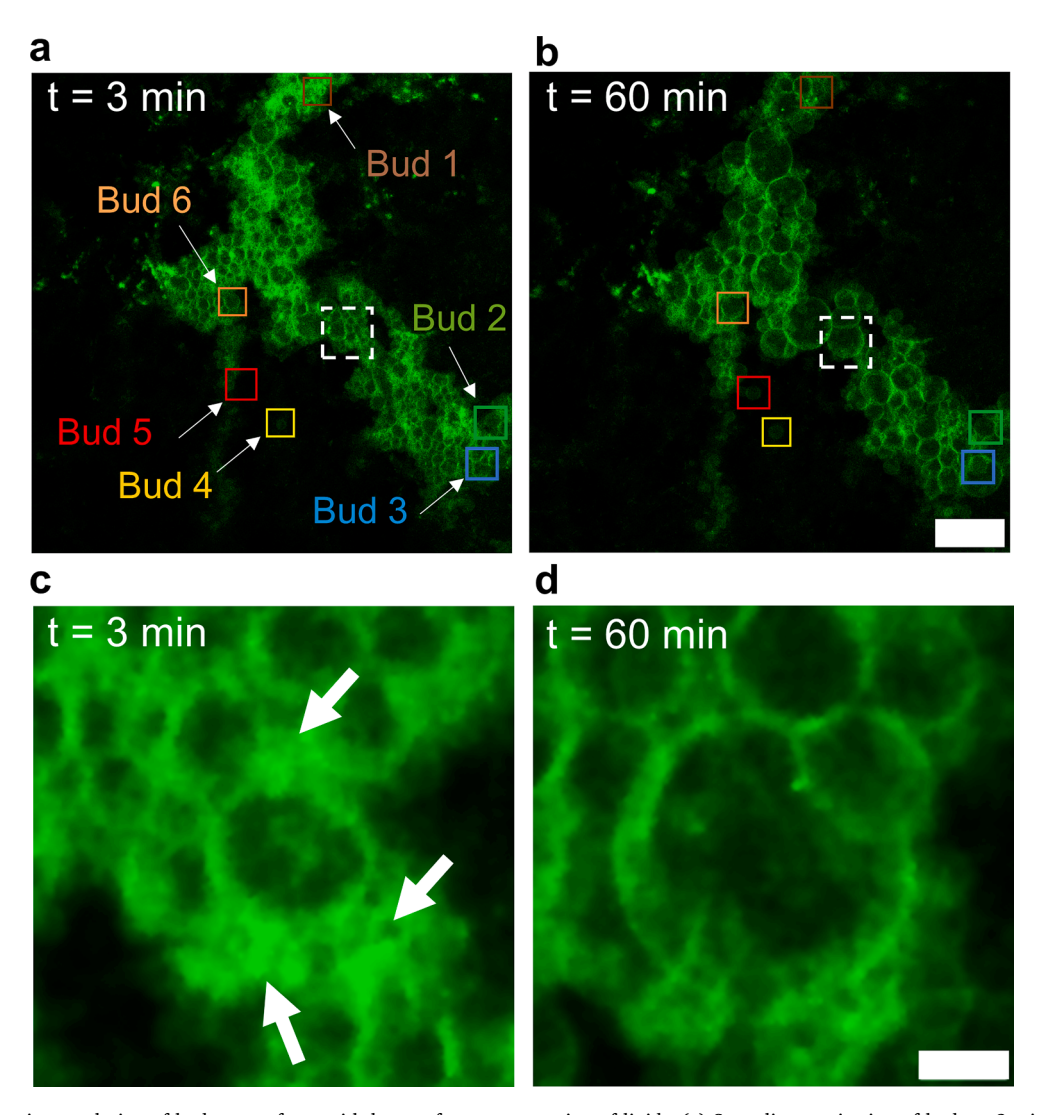


Fig. 7. Images of the time evolution of buds on surfaces with low surface concentration of lipids. (a) Sum slices projection of buds at 3 min. The colored boxes highlight buds that do not merge with their neighbors and analyzed in Fig. 8a. The white dashed box corresponds to the cluster of buds analyzed in Fig. 8b. (b) Sum slices projection of buds at 60 min. (c) Magnified image showing regions with high fluorescence intensity in the clusters at 3 min (white arrows). (d) After 60 min, the bright regions evolved into optically resolvable buds. (a,b) Scale bar 50 μm. (c,d) Scale bar 10 μm.

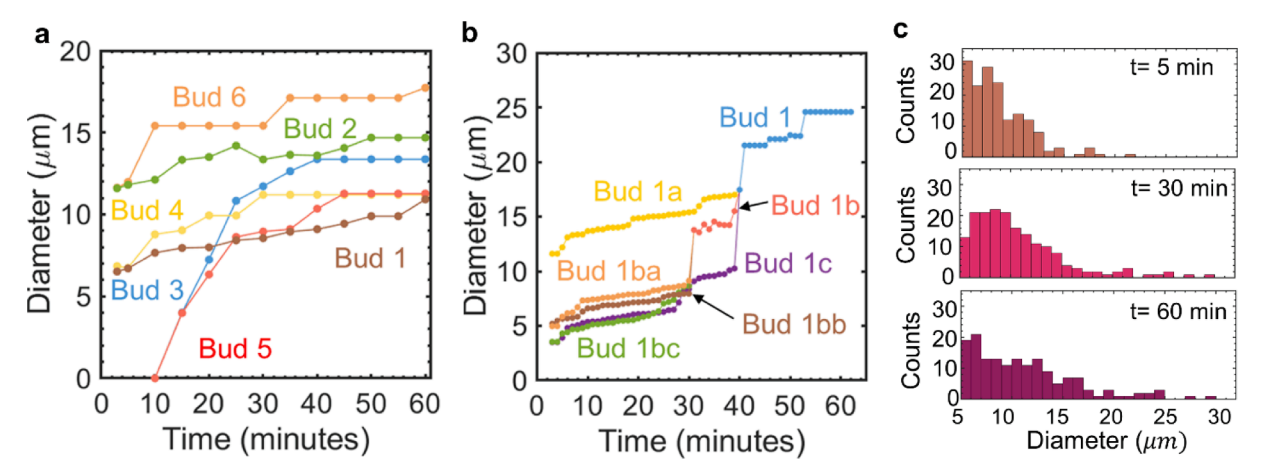


Fig. 8. Analysis of bud dynamics on surfaces with a low surface concentration of lipids. (a) Diameter versus time trajectories for the 6 buds highlighted by the colored boxes in Fig. 7. These buds increase in diameter without merging with their neighbors. (b) Diameter versus time trajectories of the cluster of 6 optically resolvable buds highlighted by the white dashed box in Fig. 7. These buds show steady increases in diameter that are punctuated by large step increases in diameter at merging events (arrows). The buds eventually become a single bud at 40 min. (c) Histogram of the diameters of the optically-resolvable buds at 5 min, 30 min, and 60 min. The evolution of the bud on the surface mirrors the stopped-time data.

Fig. 8a shows characteristic diameter versus time curves of the buds. Buds 1, 2, 4, and 6 were already micrometer in diameter at the earliest time of observation, while buds 3 and 5 emerged 15 min after we began our observation. All 6 curves show a sigmoidal shape. On average, the buds increase in diameter by 44 % over the course of 1 h. Buds spatially separated on the surface show different rates of lipid incorporation. The fastest rate of lipid incorporation was for Bud 3 at $9.7 \times 10^{-17} \, \mathrm{mol \ min^{-1}}$ and the slowest rate of incorporation was for Bud 1 at $1.9 \times 10^{-17} \, \mathrm{mol \ min^{-1}}$. These individual rates are 6 orders of magnitude lower than the rates obtained for the population level data in Fig. 5. Taken together, our results suggest that local lipid concentration on the surface impacts the kinetics of lipid incorporation since the stopped-time data was collected with four times more lipid on the surfaces compared to these experiments. This result is consistent with the expectation that the kinetics accelerates with the increased surface concentration of lipids.

Although we can discern bud emergence and diameter growth, even with sparse coverage, most buds increase in diameter and then merge with their neighbors. Fig. 8b shows zoomed images of the evolution of 5 buds shown in the white dashed box in Fig. 7a. At the initial observation time, 5 buds were present. Then Bud 1ba, Bud1bb, and Bud1bc merge at 29 min to form Bud 1b. Bud 1a, Bud1b, and Bud1c merge at 38 min to form Bud 1. All the buds clearly show an increase in their diameter due to incorporation of new lipids. Discontinuous step increases in diameter at merging events punctuates this steady increase (Fig. 8b). We note interestingly, that unlike buds separated in location, the rate of increase in diameter of these buds that are in proximity is similar to each other.

We evaluate the effects of these dynamics on the bud sizes by measuring and plotting the histogram of the diameter of the buds on the surface at 5, 30, and 60 min (Fig. 8c). We show the median diameter and the variance in Table S1. The combination of bud emergence, sigmoidal bud growth, and merging reproduces the asymmetric distribution of diameters that we observe in our stopped-time data.

To summarize, the local dynamics of the buds on the surfaces, though complex, qualitatively match the evolution of the population of GUVs. We suggest that the equal importance of bud emergence, bud diameter increase, and bud merging likely explains the inability of functions used to describe the time evolution of distributions of dispersed particles to explain the time evolution of the distributions of diameters of GUVs obtained from these thin film methods.

3.6. The budding and merging model explains the dynamics of GUVs

The underlying dynamics of the buds evolving on the surfaces are

clearly complex. Nevertheless, we can deduce that fundamental mechanisms are at work in each of the three thin film hydration methods. All three methods have similar initial yields despite the differences in surface geometry. Then, the yield increases at different rates and plateaus at different levels and times.

We rationalize these results using the thermodynamically motivated budding and merging (BNM) model for the assembly of GUVs [31]. In this model, connected surface-attached spherical nano- and micro- sized buds merge to form GUV-sized buds on the thin lipid films [31]. The lipid bilayers in a stack conform to the flat surface geometry of the substrates used for electroformation and gentle hydration and the nanoscale cylindrical geometry of the enmeshed nanoscale cylindrical fibers of nanocellulose paper used for PAPYRUS. On surfaces composed of cylindrical fibers, the change in energy for forming a spherical bud of radius R_B from a cylindrical bilayer with length L_C and radius R_C , $\Delta E_{R_B,C}$, is given by Equation 1.

$$\Delta E_{R_B,c} = \pi \kappa_B \left(8 - \frac{L_c}{R_c} \right) + 4\pi R_c \lambda - 2\pi R_c L_c \xi \tag{1}$$

On flat surfaces, the change in energy for forming a spherical bud of radius, R_B , $\Delta E_{R_B,d}$, from a flat lipid disk of radius, R_d is given by Equation 2.

$$\Delta E_{R_B,d} = 8\pi\kappa_B + 2\pi R_d \lambda - \pi R_d^2 \xi \tag{2}$$

In these equations, κ_h is the bending modulus, λ is the edge energy, and ξ is the effective adhesion contact potential of the lipid bilayer. The first term on the right-hand side measures the change in bending energy, the second term measures the change in edge energy if breaks in the bilayer must form to allow budding at a constant area, and the third term measures the change in adhesion energy to separate the bilayers. We take that the bilayers are in a stack of multiple bilayers. Thus, the effective adhesion contact potential, ξ , is that of bilayers interacting with each other. For membranes that interact via an attractive interaction potential, such as for DOPC, ξ is negative. The geometry of the nanocellulose fibers limits the maximum size of buds that can form to $R_B = \sqrt{\frac{R_c L_c}{2}}$. For the typical dimensions of a cylindrical bilayer on a nanocellulose fiber with $R_c=20~\mathrm{nm}$ and $L_c=2000~\mathrm{nm}$, the radius of the bud R_B = 100 nm. Using values of $\kappa_B = 8.5 \times 10^{-20} J, \lambda = 1 \times 10^{-11} J \, m^{-1}$, and $\xi = -1 \times 10^{-5} \, \mathrm{J} \, \mathrm{m}^{-2}$ for DOPC [40], the energy to form this bud, $\Delta E_{R_b,c} = -4750~k_BT$. Here the energy is expressed relative to the thermal energy scale 1 $k_BT = 4.11 \times 10^{-21}$ J. Inspection of Equation 2 shows that the energy for forming a spherical bud, $R_B = \frac{R_d}{2}$ from a flat bilayer of radius R_d is always positive and scales with the radius of the bud. On flat surfaces, bilayers form large, stepped sheets [30] and thus there is no apparent geometrical limit to R_d . For a GUV-sized bud with $R_B = 0.5 \, \mu m$, $\Delta E_{R_{b,d}} \approx 15,000 \, k_B T$. For a nanosized-bud with $R_B = 100 \, \text{nm}$, $\Delta E_{R_{b,d}} \approx 3580 \, k_B T$. This calculation emphasizes that the formation of buds of all sizes, including nanosized buds, is energetically costly on flat surfaces.

Once formed however, the merging of connected spherical buds on the film is energetically favorable. This is because each spherical bud, regardless of size, has a fixed positive elastic energy of $8\pi\kappa_B$ due to the bending of the membrane. Merging of N buds to form n buds reduces the total elastic energy of the system by $(N-n)8\pi\kappa_B$. Thus, for a fixed area, a film with few spherical buds of large diameters has a lower total elastic energy than a film with large numbers of spherical buds of small diameters [31].

With this thermodynamically motivated picture, we seek to explain the dynamics (Fig. 9). For all three methods, there is a source of energy above k_BT during the moment of hydration due to heats of hydration and hydrodynamic flows [41]. We thus expect buds to form on the lipid films regardless of the geometry of the films or the method. Assuming a Boltzmann like distribution, $N \propto \exp\left(-\frac{\Delta E_{R_g}}{W}\right)$ where W is the energy from external sources, we expect to have many more small buds than large buds on the films. Since we prepared our surfaces identically, the similar yield of GUV-sized buds obtained within 1 min after hydration for all three methods is consistent with this expectation (Fig. 9).

During the transient period, the time evolution of yields diverges for the three methods. For PAPYRUS, since the change in free energy for the formation of nanoscale spherical buds from nanoscale cylindrical bilayers is negative, additional nanobuds form spontaneously and merge. The steady increase in diameter of GUV buds (Fig. 8a) without any visible merging is consistent with nanoscale buds merging with the optically resolvable micrometer-scale GUV buds. Order of magnitude estimates reveals the reasonableness of this picture. To obtain a rate of lipid incorporation of 9.7 \times 10^{-17} mol min $^{-1}$, approximately three nanobuds with $R_B=100$ nm must merge per second with the GUV-sized bud. Approximately 25 nanobuds with $R_B=100$ nm must merge with each other to form a single 1 μm diameter bud. Assuming a rate of merging of 3 nanobuds per second, a 1 μm diameter bud can emerge every 10 s. We propose that the steady state plateau in yield that we observe occurs when the nanoscale buds are depleted on the surface.

In contrast, gentle hydration shows both limited evolution of yields and limited increase in bud diameters compared to PAPYRUS. Like PAPYRUS, gentle hydration occurs in quiescent solution and does not have any obvious sources of energy input. However, unlike PAPYRUS, the formation of additional buds after the initial moment of hydration from flat bilayers requires the input of energy. We expect only limited nanoscale buds to be available to increase the sizes of the buds through merging. Thus, the limited evolution of GUVs after the initial moment of hydration for gentle hydration is rational.

For electroformation, the electric field inputs energy by acting on the charges of the lipid headgroups and the solution [25,42–45]. Additionally, merging of buds is said to be enhanced due to the action of an electric field [46]. We propose that the active input of energy from the electric field and the complex effects of the electric field on merging is consistent with the complex time evolution of the buds for electroformation (Fig. 5f) compared to PAPYRUS and gentle hydration (Fig. 5d, e). Obtaining further detailed insights into the dynamics for electroformation [47–49] will require a deeper understanding of the effects of the electric field on the thin lipid film and the aqueous buffer.

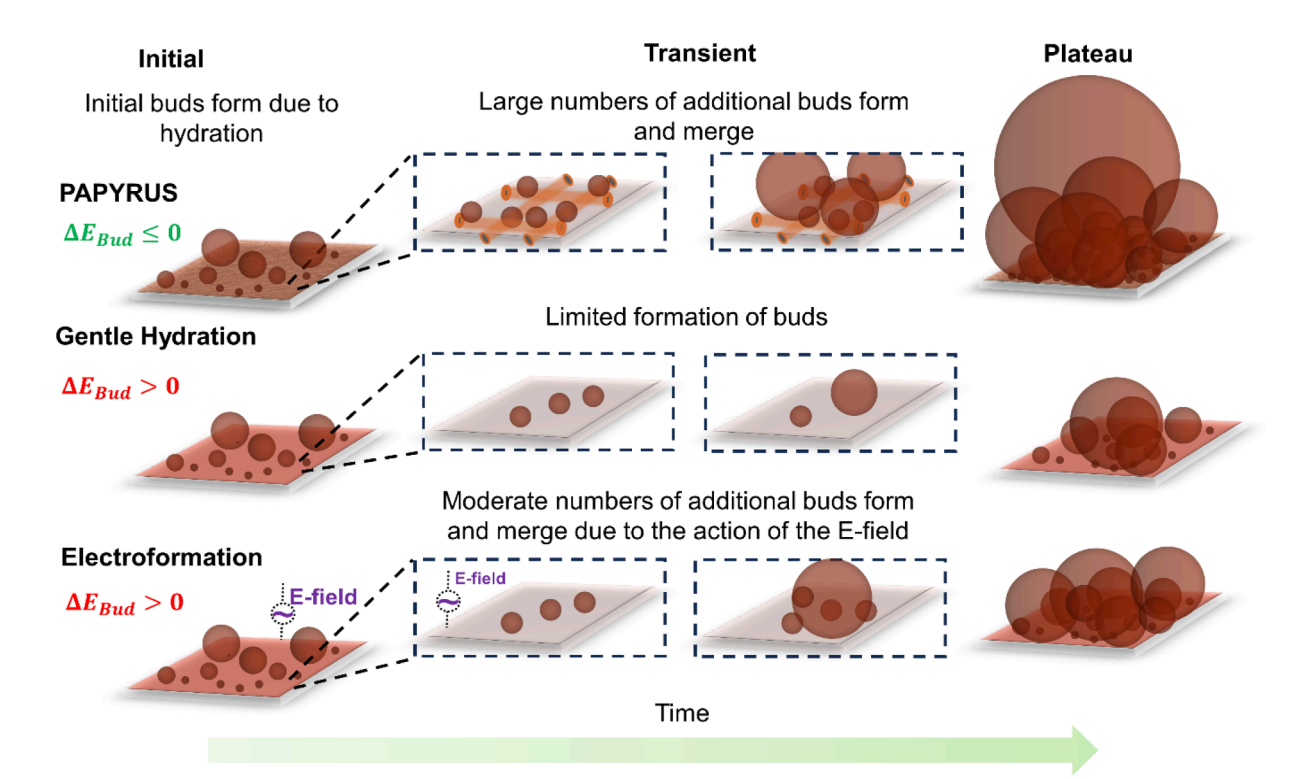


Fig. 9. Proposed explanation for the observed dynamics. The free energy of formation of buds is negative for PAPYRUS and positive for gentle hydration and electroformation. At the initial phase, the expected similar energies due to the heat of hydration and the hydrodynamics of the buffer flows causes the formation of similar numbers of buds on all three surfaces. The behavior differs at the transient due to differences in energy of budding on the surfaces and the available sources of energy to do work. Large numbers of additional buds form and merge to form large buds for PAPYRUS due to the negative free energy change of budding of lipid bilayers on nanoscale cylindrical fibers. Limited number of buds form and merge for gentle hydration because the free energy change of budding is positive for lipid bilayers on flat surfaces. The electric field can do work to form moderate number of buds for electroformation despite the positive free energy change of budding. Due to the differences in numbers of buds that form for the three methods, the yield at the plateau and the number of GUV buds with large diameters is different. Schematics are not to scale.

Depletion of nanobuds can explain the eventual decrease in the rate of incorporation of lipids in the populations of GUVs. Our dynamic data however reveals that there must be barriers to bud merging since the rate of merging of GUV-sized buds decreases and eventually stops despite the apparent energetic favorability of continued merging. GUV-sized buds generally become larger with time. Many more lipid molecules must rearrange when large buds merge compared to when small buds merge. We speculate that the increase in viscous dissipation from moving large sections of membranes and volumes of buffer could balance the energy gain of merging. This results in the slowing down of the rate of merging of neighboring GUV-sized buds and the apparent kinetic tapping of the configuration of GUV-sized buds after 120 min.

4. Conclusions

Previous approaches have reported qualitative or semi-quantitative measures of the yields of GUVs [1,2]. Recent quantitative measures of the molar yield and size distributions of populations of GUVs have only reported static yields [31]. The development of the stopped-time technique here allows the first report of the time evolution of the molar vields and size distributions of GUVs. The results show that the time evolution of the molar yield of GUVs obtained from three thin film hydration methods, PAPYRUS, gentle hydration, and electroformation, is sigmoidal, with an initial yield, a transient, and a steady state plateau. Plotting the molar yield of GUVs $\geq 10 \ \mu m$ in diameter versus the total molar yield reveals significant differences in the dynamics between the three thin film hydration methods. The observed dynamics are consistent with the thermodynamically motivated budding and merging (BNM) model. The budding and merging model posits that GUVs assemble from thin lipid films through the formation and merging of surface-attached nano- and micro-meter scale buds.

The apparent sigmoidal evolution of the yield is qualitatively akin to other interface dominated processes such as classical nucleation and growth [36]. However, the local GUV bud dynamics on the surfaces differ from these other systems and is characterized by an increase in the variance of the size distribution with time. Looking forward, population balance models used to describe interface dominated dynamical processes [50,51], but thus far not applied to the evolution of GUVs, offer a promising theoretical framework for understanding the evolution of GUV size distributions from the local processes of bud emergence, bud diameter increase, and bud merging.

Future directions using the stopped-time technique could study the dynamics of the assembly of GUVs from membranes composed of mixtures of lipids with different headgroups, chain saturations, chain lengths, and with different sterol contents. The composition of the membranes affects properties such as the bending rigidity, edge energy, and membrane adhesion. These changes will likely result in differences in the rate of lipid incorporation, the steady state yields, and the distribution of sizes due to changes in the free energy cost of forming spherical buds.

Finally, from a practical perspective, our data shows that the evolution of sizes is mostly complete within 120 min of the initial hydration. The data thus provides a pathway to rationally tailor the production of GUVs with specific sizes for applications.

Declaration of competing interest

The authors declare that they have no known competing financial interests or personal relationships that could have appeared to influence the work reported in this paper.

Data availability

Data will be made available on request.

Acknowledgements

This work was funded by the National Science Foundation through NSF CAREER DMR-1848573. The data in this work was collected, in part, with a confocal microscope acquired through the National Science Foundation MRI Award Number DMR-1625733.

Appendix A. Supplementary data

Supplementary data to this article can be found online at https://doi.org/10.1016/j.jcis.2024.02.022.

References

- C. Has, P. Sunthar, A comprehensive review on recent preparation techniques of liposomes, J. Liposome Res. (2019) 1–30, https://doi.org/10.1080/ 08982104 2019 1668010
- [2] K.S. Nair, H. Bajaj, Advances in giant unilamellar vesicle preparation techniques and applications, Adv. Colloid Interface Sci. 318 (2023) 102935, https://doi.org/ 10.1016/j.cis.2023.102935.
- [3] N. Dolder, P. Müller, C. von Ballmoos, Experimental platform for the functional investigation of membrane proteins in giant unilamellar vesicles, Soft Matter 18 (2022) 5877–5893, https://doi.org/10.1039/d2sm00551d.
- [4] J. Steinkühler, R.L. Knorr, Z. Zhao, T. Bhatia, S.M. Bartelt, S. Wegner, R. Dimova, R. Lipowsky, Controlled division of cell-sized vesicles by low densities of membrane-bound proteins, Nat. Commun. 11 (2020) 1–11, https://doi.org/ 10.1038/s41467-020-14696-0.
- [5] W. Xin, H. Wu, G.M. Grason, M.M. Santore, Switchable positioning of plate-like inclusions in lipid membranes: elastically mediated interactions of planar colloids in 2D fluids, Sci. Adv. 8 (2021) eabf1943.
- [6] M. Morita, N. Noda, Membrane shape dynamics-based analysis of the physical properties of giant unilamellar vesicles prepared by inverted emulsion and hydration techniques, Langmuir 37 (2021) 2268–2275, https://doi.org/10.1021/ acs.langmuir.002698
- [7] V.N. Ngassam, W.C. Su, D.L. Gettel, Y. Deng, Z. Yang, N. Wang-Tomic, V. P. Sharma, S. Purushothaman, A.N. Parikh, Recurrent dynamics of rupture transitions of giant lipid vesicles at solid surfaces, Biophys. J. 120 (2021) 586–597, https://doi.org/10.1016/j.bpj.2021.01.006.
- [8] W.C. Su, J.C.S. Ho, D.L. Gettel, A.T. Rowland, C.D. Keating, A.N. Parikh, Kinetic control of shape deformations and membrane phase separation inside giant vesicles, Nat. Chem. (2023).
- [9] E. Cho, Y. Lu, Compartmentalizing cell-free systems: toward creating life-like artificial cells and beyond, ACS Synth. Biol. 9 (2020) 2881–2901, https://doi.org/ 10.1021/acssynbio.0c00433.
- [10] X. Wang, H. Du, Z. Wang, W. Mu, X. Han, Versatile phospholipid assemblies for functional synthetic cells and artificial tissues, Adv. Mater. 33 (2021) 1–23, https://doi.org/10.1002/adma.202002635.
- [11] T. Litschel, B. Ramm, R. Maas, M. Heymann, P. Schwille, Beating vesicles: encapsulated protein oscillations cause dynamic membrane deformations, Angew. Chem. Int. Ed. 57 (2018) 16286–16290, https://doi.org/10.1002/anie.201808750.
- [12] L. van de Cauter, L. van Buren, G.H. Koenderink, K.A. Ganzinger, Exploring giant unilamellar vesicle production for artificial cells – current challenges and future directions, Small Methods (2023), https://doi.org/10.1002/smtd.202300416.
- [13] P. Stano, F. Mavelli, Protocells models in origin of life and synthetic biology, Life 5 (2015) 1700–1702, https://doi.org/10.3390/life5041700.
- [14] A. Lopez, M. Fiore, Investigating prebiotic protocells for a comprehensive understanding of the origins of life: a prebiotic systems chemistry perspective, Life 9 (2019)
- [15] I. Gözen, E.S. Köksal, I. Põldsalu, L. Xue, K. Spustova, E. Pedrueza-Villalmanzo, R. Ryskulov, F. Meng, A. Jesorka, Protocells: Milestones and Recent Advances, Small (2022) 2106624. https://doi.org/10.1002/smll.202106624.
- [16] I. Buttino, G. De Rosa, Y. Carotenuto, A. Ianora, A. Fontana, F. Quaglia, M.I. La Rotonda, A. Miralto, Giant liposomes as delivery system for ecophysiological studies in copepods, J. Exp. Biol. 209 (2006) 801–809, https://doi.org/10.1242/ jeb.02068.
- [17] L. Teixeira, R. Rossi, G.B. Nunes, C. Rodrigues, H. De Rossi, P. Helena, M. Fábio, G. Nogueira, P. Henrique, B. Aoki, G.Z. Mingoti, Use of giant unilamellar lipid vesicles as antioxidant carriers in in vitro culture medium of bovine embryos, Sci. Rep. (2022) 1–12, https://doi.org/10.1038/s41598-022-14688-8.
- [18] L. Le Nagard, A.T. Brown, A. Dawson, V.A. Martinez, W.C.K. Poon, M. Staykova, Encapsulated bacteria deform lipid vesicles into flagellated swimmers, PNAS 119 (2022).
- [19] M. Morita, K. Katoh, N. Noda, Direct observation of bacterial growth in giant unilamellar vesicles: a novel tool for bacterial cultures, ChemistryOpen 7 (2018) 845–849, https://doi.org/10.1002/open.201800126.
- [20] T. Trantidou, L. Dekker, K. Polizzi, O. Ces, Y. Elani, Functionalizing cell-mimetic giant vesicles with encapsulated bacterial biosensors, Interface Focus 8 (2018) 20180024. https://royalsocietypublishing.org/doi/10.1098/rsfs.2018.0024.
- [21] F. Lussier, O. Staufer, I. Platzman, J.P. Spatz, Can bottom-up synthetic biology generate advanced drug-delivery systems? Trends Biotechnol. 39 (2021) 445–459, https://doi.org/10.1016/j.tibtech.2020.08.002.

- [22] D.L. Perrier, L. Rems, P.E. Boukany, Lipid vesicles in pulsed electric fields: Fundamental principles of the membrane response and its biomedical applications, Adv. Colloid Interface Sci. 249 (2017) 248–271, https://doi.org/10.1016/j. cis 2017 04 016
- [23] A.D. Bangham, M.M. Standish, J.C. Watkins, Diffusion of univalent ions across the lamellae of swollen phospholipids, J. Mol. Biol. 13 (1965) 238–252, https://doi. org/10.1016/S0022-2836(65)80093-6.
- [24] J.P. Reeves, R.M. Dowben, Formation and properties of thin-walled phospholipid vesicles, J. Cell. Physiol. 73 (1969) 49–60, https://doi.org/10.1002/ jcp.1040730108.
- [25] D.S. Dimitrov, M.I. Angelova, Lipid swelling and liposome formation mediated by electric fields, Bioelectrochem. Bioenerg. 253 (1988) 323–336.
- [26] V. Pereno, D. Carugo, L. Bau, E. Sezgin, J. Bernardino De La Serna, C. Eggeling, E. Stride, Electroformation of giant unilamellar vesicles on stainless steel electrodes, ACS Omega 2 (2017) 994–1002, https://doi.org/10.1021/ accomega 6b00305
- [27] M. Angelova, S. Soleau, P. Méléard, Preparation of giant vesicles by external AC electric fields. Kinetics and applications, Progr Colloid Polym Sci 89 (1992) 127–131, https://doi.org/10.1007/BFb0116295.
- [28] K.S. Horger, D.J. Estes, R. Capone, M. Mayer, Films of agarose enable rapid formation of giant liposomes in solutions of physiologic ionic strength, J. Am. Chem. Soc. 131 (2009) 1810–1819, https://doi.org/10.1021/ja805625u.
- [29] A. Weinberger, F.C. Tsai, G.H. Koenderink, T.F. Schmidt, R. Itri, W. Meier, T. Schmatko, A. Schröder, C. Marques, Gel-assisted formation of giant unilamellar vesicles, Biophys. J. 105 (2013) 154–164, https://doi.org/10.1016/j. bbi 2013 05 024
- [30] A. Cooper, V. Girish, A.B. Subramaniam, Osmotic pressure enables high-yield assembly of giant vesicles in solutions of physiological ionic strengths, Langmuir 39 (2023) 5579–5590, https://doi.org/10.1021/acs.langmuir.3c00457.
- [31] J. Pazzi, A.B. Subramaniam, Nanoscale curvature promotes high yield spontaneous formation of cell-mimetic giant vesicles on nanocellulose paper, ACS Appl. Mater. Interfaces 12 (2020) 56549–56561, https://doi.org/10.1021/acsami.0c14485.
- [32] M.A.S. Karal, M. Ahmed, V. Levadny, M. Belaya, M.K. Ahamed, M. Rahman, M. M. Shakil, Electrostatic interaction effects on the size distribution of self-assembled giant unilamellar vesicles, Phys. Rev. E 101 (2020) 1–11, https://doi.org/10.1103/PhysRevE.101.012404.
- [33] K.J. Storslett, S.J. Muller, Evaluation and comparison of two microfluidic size separation strategies for vesicle suspensions separation strategies for vesicle suspensions, Biomicro 11 (2017) 034112.
- [34] V. Girish, J. Pazzi, A. Li, A.B. Subramaniam, Fabrics of diverse chemistries promote the formation of giant vesicles from phospholipids and amphiphilic block copolymers, Langmuir 35 (2019) 9264–9273, https://doi.org/10.1021/acs. langmuir.9b01621.

- [35] J. Pazzi, M. Xu, A.B. Subramaniam, Size distributions and yields of giant vesicles assembled on cellulose papers and cotton fabric, Langmuir 35 (2019) 7798–7804, https://doi.org/10.1021/acs.langmuir.8b03076.
- [36] N.T.K. Thanh, N. Maclean, S. Mahiddine, Mechanisms of nucleation and growth of nanoparticles in solution, Chem. Rev. 114 (2014) 7610–7630.
- [37] P.W. Voorhees, The theory of ostwald ripening, J. Stat. Phys. 38 (1985) 231–252.
- [38] P.T. Spicer, Sotiris E. Pratsinis, Coagulation and fragmentation: universal steadystate particle-size distribution, AIChE J. 42 (1996) 1612–1620.
- [39] C. Huang, D. Quinn, Y. Sadovsky, S. Suresh, K.J. Hsia, Formation and size distribution of self-assembled vesicles, PNAS 114 (2017) 2910–2915, https://doi. org/10.1073/pnas.1702065114.
- [40] J.N. Israelachvili, Intermolecular and Surface Forces, third ed., Academic Press, Waltham, MA, 2011.
- [41] D.D. Lasic, F.J. Martin, On the mechanism of vesicle formation, Biochem. J 256 (1988) 1–11, https://doi.org/10.1016/S0376-7388(00)80317-8.
- [42] Q. Li, X. Wang, S. Ma, Y. Zhang, X. Han, Electroformation of giant unilamellar vesicles in saline solution, Colloids Surf. B Biointerfaces 147 (2016) 368–375, https://doi.org/10.1016/j.colsurfb.2016.08.018.
- [43] J. Seiwert, P.M. Vlahovska, Instability of a fluctuating membrane driven by an ac electric field, Phys. Rev. E Stat. Nonlin. Soft Matter Phys. 87 (2013) 1–13, https:// doi.org/10.1103/PhysRevE.87.022713.
- [44] P. Sens, H. Isambert, Undulation instability of lipid membranes under an electric field, Phys. Rev. Lett. 88 (2002) 128102, https://doi.org/10.1103/ PhysRevLett.88.128102.
- [45] R. Dimova, K.A. Riske, S. Aranda, N. Bezlyepkina, R.L. Knorr, R. Lipowsky, Giant vesicles in electric fields, Soft Matter 3 (2007) 817–827, https://doi.org/10.1039/ b703580b.
- [46] Y.M.S. Micheletto, C.M. Marques, N.P. Da Silveira, A.P. Schroder, Electroformation of giant unilamellar vesicles: investigating vesicle fusion versus bulge merging, Langmuir 32 (2016) 8123–8130, https://doi.org/10.1021/acs.langmuir.6b01679.
- [47] Z. Liang, M. Chen, X. Yi, W. Zhu, Membrane-tension-dominated growth mechanism and size modulation of giant unilamellar vesicles in electroformation, J. Mech. Phys. Solids 170 (2023).
- [48] T.J. Politano, V.E. Froude, B. Jing, Y. Zhu, AC-electric field dependent electroformation of giant lipid vesicles, Colloids Surf. B Biointerf. 79 (2010) 75–82, https://doi.org/10.1016/j.colsurfb.2010.03.032.
- [49] S.E. Ghellab, W. Mu, Q. Li, X. Han, Prediction of the size of electroformed giant unilamellar vesicle using response surface methodology, Biophys. Chem. 253 (2019) 106217, https://doi.org/10.1016/j.bpc.2019.106217.
- [50] D. Ramkrishna, M.R. Singh, Population balance modeling: Current status and future prospects, Annu. Rev. Chem. Biomol. Eng. 5 (2014) 123–146, https://doi. org/10.1146/annurey-chembioeng-060713-040241.
- [51] B.J. McCoy, A new population balance model for crystal size distributions: Reversible, size-dependent growth and dissolution, J. Colloid Interface Sci. 240 (2001) 139–149. https://doi.org/10.1006/jcis.2001.7629.